Intrinsic viscosity and the electrical polarizability of arbitrarily shaped objects

Marc L. Mansfield,[1,*] Jack F. Douglas,[2,*] and Edward J. Garboczi[3]
[1]*Department of Chemistry and Chemical Biology, Stevens Institute of Technology, Hoboken, New Jersey 07030*
[2]*Polymers Division, National Institute of Standards and Technology, Gaithersburg, Maryland 20899*
[3]*Building Materials Division, National Institute of Standards and Technology, Gaithersburg, Maryland 20899*
(Received 26 February 2001; published 20 November 2001)

The problem of calculating the electric polarizability tensor α_e of objects of arbitrary shape has been reformulated in terms of path integration and implemented computationally. The method simultaneously yields the electrostatic capacity C and the equilibrium charge density. These functionals of particle shape are important in many materials science applications, including the conductivity and viscosity of filled materials and suspensions. The method has been validated through comparison with exact results (for the sphere, the circular disk, touching spheres, and tori), it has been found that 10^6 trajectories yield an accuracy of about four and three significant figures for C and $\boldsymbol{\alpha}_\mathbf{e}$, respectively. The method is fast: For simple objects, 10^6 trajectories require about 1 min on a PC. It is also versatile: Switching from one object to another is easy. Predictions have also been made for regular polygons, polyhedra, and right circular cylinders, since these shapes are important in applications and since numerical calculations of high stated accuracy are available. Finally, the path-integration method has been applied to estimate transport properties of both linear flexible polymers (random walk chains of spheres) and lattice model dendrimer molecules. This requires probing of an ensemble of objects. For linear chains, the distribution function of C and of the trace $(\boldsymbol{\alpha}_\mathbf{e})$, are found to be universal in a size coordinate reduced by the chain radius of gyration. For dendrimers, these distribution functions become increasingly sharp with generation number. It has been found that C and α_e provide important information about the distribution of molecular size and shape and that they are important for estimating the Stokes friction and intrinsic viscosity of macromolecules.

DOI: 10.1103/PhysRevE.64.061401 PACS number(s): 66.20.+d, 41.20.−q

I. INTRODUCTION

There are many applications in materials science and electromagnetism involving boundary value problems for which the boundaries have complicated shapes [1]. Examples include the computation of the electrostatic capacity, Smoluchowski rate constant and translational friction coefficient of arbitrary objects; [2–5] the fluid discharge through a pipe of arbitrary cross section; [6] and the calculation of virial coefficients for the leading order concentration dependence of effective material properties of suspensions and composites containing particles of complex shape [7,8]. Moreover, the far-field scattering of objects by electromagnetic radiation [9–11] and sound [12] and the propagation of electromagnetic [13] and acoustic radiation [14] through apertures all involve the calculation of the electrostatic capacity and electric and magnetic polarizability of complex shapes. These same quantities arise in the virial coefficient calculations [7] for the transport properties of inhomogeneous materials. Therefore, these calculations have many applications to problems involving the scattering of light or sound from particles having elaborate structure (e.g., snowflakes, atmospheric dust, particle aggregates in liquid dispersions, and macromolecules in solution). Moreover, there is an extensive literature devoted to using these shape dependent energy functionals to classify particle shape [2,15]. Such functionals have already been used to characterize the topology of polymer chains [16] and we expect that they should be useful in identifying more subtle topological features such as the knot complexity of knotted polymers and the genus and other topological characteristics of membranes [1]. At present, numerical approaches based on differential equation or finite element methods have not been generally effective when the boundary is intricate. The numerical path-integration methods discussed below will make this important class of problems more accessible.

In the present paper, we extend previous numerical path-integration calculations of the electrostatic capacity of arbitrarily shaped objects [2–4] to the calculation of the electrical polarizability tensor $\boldsymbol{\alpha}_\mathbf{e}$ and apply these calculations to the estimation of the intrinsic viscosity $[\eta]$ and intrinsic conductivity $[\sigma]_\infty$ of suspensions of rigid particles and highly conductive particles, respectively. The probabilistic calculation also yields the electrostatic capacity C, providing an estimate of the friction coefficient of a Brownian particle and the Smoluchowski rate constant for the particle undergoing a diffusion-limited reaction [1–4]. This simple and general computational method yields high accuracy when compared with results for exactly soluble particle geometries. It should have many applications both in materials science and in biophysics, where the properties of inhomogeneous materials and of particles of complex shape are of interest.

II. REVIEW OF HYDRODYNAMIC-ELECTROSTATIC PROPERTY RELATIONS

There are many analogies relating the hydrodynamics of suspensions and flowing fluids, the electrostatic properties of conducting and insulating objects, and the elasticity of com-

*Authors to whom correspondence should be addressed.

posite materials and elastic shafts under torsion. For example, the hydrodynamic mass tensor **M** of particles of general shape is proportional to the magnetic polarizability tensor $\boldsymbol{\alpha}_{\mathbf{m}}$ of a conducting particle having the same shape [7,10,17]. (The hydrodynamic mass tensor is the true mass plus the ''virtual mass'' associated with induced fluid motion accompanying object movement [18]) The friction coefficient of a plate of general shape translating normal to its plane and the force required to displace the interface of an elastic material are proportional to the electrostatic capacity of the plate C [19]. The rotational friction coefficient of an axisymmetric body is proportional to the component of the hydrodynamic mass tensor **M** about the axis of symmetry [20] and generalized axisymmetric potential theory indicates that this hydrodynamic mass component is proportional to the capacity of the object rotated symmetrically into two higher spatial dimensions [2,21]. The problem of calculating the torsional rigidity and the elastic strain field within a twisted elastic bar is mathematically equivalent to calculating the fluid flux and velocity field for the Poisseuille flow flux and velocity field in a pipe of arbitrary cross section [6,15] and this problem in turn reduces to the solution of Poisson's equation and corresponding electrostatic applications [22]. The flux of an inviscid and viscous fluid through holes in a planar interface is governed by the capacity and hydrodynamic mass of the holes, respectively [23,24]. The virtual mass density of a flowing dispersion of bubbles is exactly related to the conductivity of a dispersion of insulating particles where the hydrodynamic-electrostatic analogy holds for arbitrary concentrations [25]. Rayleigh also pointed out that the field equations governing an incompressible solid at equilibrium are identical to those for the steady flow of a Newtonian fluid where particle displacement replaces velocity and shear modulus replaces viscosity. Thus, the modulus increment of a solid and the viscosity increment of a fluid, both arising from identical dispersions of rigid inclusions, are identical [26]. This is just a sampling of the many relations that exist between these field theories.

There are also many *approximate* electrostatic-hydrodynamic relations of this kind, which are useful in estimating properties dependent on particle shape. In the present paper, we are particularly interested in two approximations, one relating the electrical polarizability tensor $\boldsymbol{\alpha}_{\mathbf{e}}$ of a conducting object to the intrinsic viscosity $[\eta]$ of a suspension of rigid particles having the same shape [7], and the other relating the electrostatic capacity C of a conducting particle and the translational friction coefficient f of a Brownian particle having the same shape [2,3,5]. The friction coefficient and intrinsic viscosity are widely used in macromolecular characterization, and these hydrodynamic-electrostatic analogies permit their estimation from numerical calculations of $\boldsymbol{\alpha}_{\mathbf{e}}$ and C via probabilistic path-integration methods. We briefly review the definition of these quantities to establish our notation and the units utilized in our computations below.

The viscosity of a dilute particle dispersion of rigid particles can be developed formally in a power series in the particle volume fraction ϕ,

$$\eta(\text{dispersion}) = \eta(\text{dispersing fluid})\{1+[\eta]\phi+O(\phi^2)\}, \tag{1}$$

(Since this expansion is analogous to the virial power series for the pressure of a nonideal gas, we refer to it as a ''virial expansion'' and to its coefficients as ''virial coefficients.'' [7]) The first virial coefficient $[\eta]$ is independent of interparticle interaction and is conventionally called the ''intrinsic viscosity'' in the rheology literature. Similarly, we can define a virial expansion for the electrical conductivity of a dispersion of randomly dispersed and oriented particles

$$\sigma(\text{dispersion}) = \sigma(\text{dispersing fluid})\{1+[\sigma]\phi+O(\phi^2)\}, \tag{2}$$

The ''intrinsic conductivity'' [7,8] of a dispersion of particles that are highly conducting relative to the dispersing fluid (metal flakes in a polymer matrix) is denoted $[\sigma]_\infty$ and for insulating particles in a relatively conductive fluid (oil particles in salt water) the leading virial coefficient is denoted $[\sigma]_0$. The refractive index, thermal conductivity, dielectric constant, magnetic permeability and other transport properties can be developed in the same type of virial expansion [7,8,27–29]

When an electric field E is applied to a medium containing highly conducting particles, a charge distribution develops on the particles. The far-field disturbance is dipolar and this dipolar field modifies the effective conductivity of the dispersion. The induced electric dipole moment μ of a perfectly conducting particle is determined by the electrical polarizability tensor $\boldsymbol{\alpha}_{\mathbf{e}}$ [30],

$$\mu = (1/4\pi)\boldsymbol{\alpha}_{\mathbf{e}}\cdot E, \tag{3}$$

and the magnetic moment μ_m is similarly related to the magnetic polarizability α_m and the magnetic field **M**. These induced dipoles for a dilute dispersion of randomly oriented conducting particles are invariant to the macroscopic orientation of the material so that the virial coefficient for the conductivity is invariant to particle orientation. In particular, the intrinsic conductivity $[\sigma]_\infty$ is proportional to the trace of the electrical polarizability tensor [7,31]

$$[\sigma]_\infty = [\text{tr}(\boldsymbol{\alpha}_{\mathbf{e}})/dV_p], \tag{4}$$

where V_p is the particle volume and d is the spatial dimension, and the virial coefficient for insulating particles $[\sigma]_0$ corresponds to Eq. (4) with $\boldsymbol{\alpha}_{\mathbf{m}}$ replacing $\boldsymbol{\alpha}_{\mathbf{e}}$ (up to a sign convention). For spheres, Maxwell [32] showed

$$[\sigma(\text{conducting sphere})]_\infty = 3, \tag{5a}$$

$$[\sigma(\text{insulating sphere})]_0 = -3/2, \tag{5b}$$

while for d-dimensional hyperspheres, Sangani [33] obtained

$$[\sigma(\text{conducting sphere})]_\infty = d, \tag{5c}$$

and

$$[\sigma(\text{insulating sphere})]_\infty = -d(d-1). \tag{5d}$$

The imposition of a shear field to a dilute dispersion of rigid particles induces a stress dipole (''stresslet'') field [34] that modifies the effective viscosity of the dispersion. The intrinsic viscosity is obtained as an angular average of the tensor field describing the perturbation of the flow field by the particle inclusion. Douglas and Garboczi [7] noted that a formal angular averaging of the stress dipole describing the hydrodynamic interaction implies $[\eta] \propto [\sigma]_\infty$ since the angular average of the Green's function of the Stokes equation is the Green's function of Laplace's equation. The constant of proportionality can be fixed from the known result for d-dimensional hyperspheres [35],

$$[\eta] = (d+2)/2. \tag{6}$$

Along with Eq. (5c) this gives the following angular averaging approximation [7]:

$$[\eta] \approx [(d+2)/2d][\sigma]_\infty . \tag{7}$$

The approximation Eq. (7) has been examined for cases in which exact results are known: triaxial ellipsoids having arbitrary asymmetry [36], spherical dumbbell particles at arbitrary separation [7], and elliptical particles in two dimensions [7]. It has also been examined by finite element calculations for a wide range of both asymmetric (cube dumbbell over a range of fixed separations, circular and rectangular cylinders) and symmetric shapes (''sponge,'' square ring, square hollow tube, ''jacks'') selected to have high electrical polarizabilities and to represent general classes of particle shapes [7]. Results for all these cases are illustrated in Figs. 1(a) and Fig. 1(b) for $d=3$ and $d=2$, respectively. Filled circles denote exact results and open circles indicate finite element calculations. Solid lines indicate Eq. (7) and the broken line in Fig. 1(a) corresponds to the ratio $[\eta]/[\sigma]_\infty = 0.8$, the limit of needle and plate ellipsoids of revolution [7]. A compilation of $[\eta]/[\sigma]_\infty$ over extensive data for ellipsoids of revolution gives

$$[\eta] \approx (0.79 \pm 0.04)[\sigma]_\infty , \tag{8}$$

in three dimensions. The uncertainty interval indicates the maximum deviation from the average [7]. All finite element data for the range of shapes indicated above and exact data for other shapes are consistent with Eq. (8). It is apparent from Fig. 1 that a better approximation is obtained by using the prefactor 0.8 for slender particles and $5/6 \cong 0.833$ for less symmetric ''globular'' shapes [37]. Thus, although Eq. (7) is not exact, it gives an estimate of $[\eta]$ valid to about 5%.

Results in two dimensions suggest that Eq. (7) may be exact in that case. For instance, it holds exactly for elliptical shapes [see Fig. 1(b)] and is also within the limit of numerical uncertainty for finite-element calculations on rectangular shapes [7]. This conjecture requires further investigation, and is significant because ''quasi-two-dimensional suspensions'' can be created by dispersing particles at liquid interfaces [38] and because two-dimensional suspensions have been studied by simulation [39].

As defined above, $[\eta]$ and $[\sigma]$ are dimensionless. However, the intrinsic viscosity is conventionally defined (especially in the polymer science literature) relative to the mass concentration rather than the volume fraction ϕ. Therefore, the conventional intrinsic viscosity is $[\eta]_M = (V_p/M)[\eta]$ for M the mass of the body.

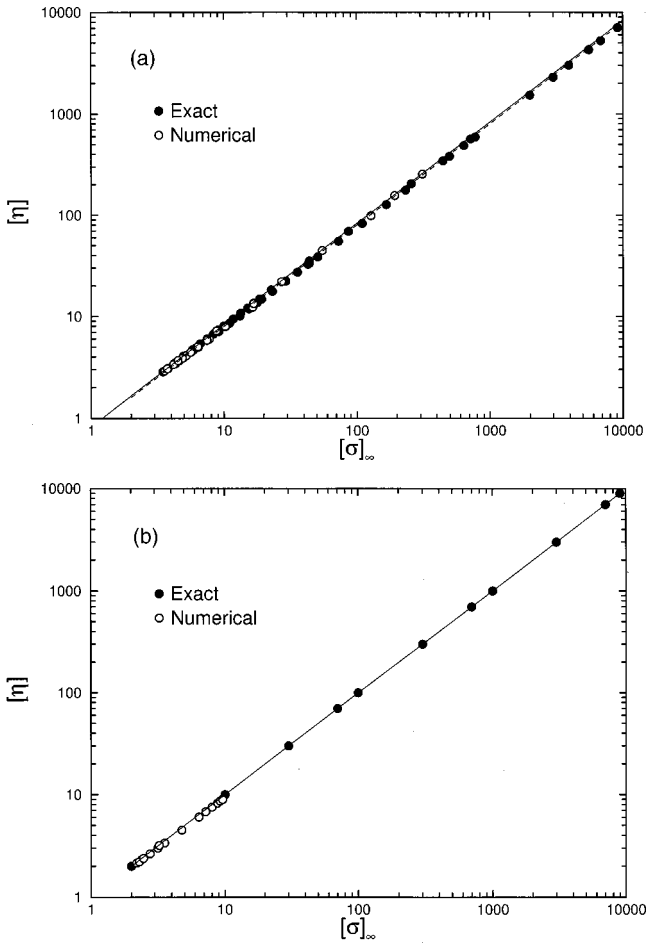

FIG. 1. Intrinsic viscosity versus intrinsic conductivity of conducting particles. Solid lines denote the angular averaging prediction of Garboczi and Douglas [7], Eq. (7). The dashed line indicates the exact result for extended needle- and plate-shaped ellipsoids of revolution. (a) Exact (●) and finite element results (○) in three dimensions. Exact results are for triaxial ellipsoids, ellipsoids of revolution [7,36], and dumbbells over a range of separations. The finite element calculations are for rectangular parallelepipeds, circular cylinders, ''jacks,'' ''sponges,'' square ring, dumbbell of cubes (''dice''), square hollow tubes in three dimensions and rectangles, a spherical lens and touching circles in two dimensions. (b) Exact (●) and finite element results (○) in two dimensions. Exact results are for ellipses and finite element calculations correspond to rectangular and polygonal regions.

A particle moving in a fluid induces motion in the fluid even in the absence of fluid viscosity. The far-field disturbance created by this motion is described by a dipolar field. The mass of the moving particle becomes equivalent to a hydrodynamic effective mass tensor $\mathbf{M}$ that is the sum of the bare mass and a ''virtual mass'' tensor $\mathbf{W}$,

$$\mathbf{M} = V_p \mathbf{I} + \mathbf{W}, \tag{9}$$

where I is the identity matrix (the density of the particle and fluid are assumed to equal unity for simplicity of discussion here). It has been shown rigorously [9,17] that $\mathbf{M}=-\boldsymbol{\alpha}_{\mathbf{m}}$ so that the exact hydrodynamic-electrostatic analogy $[\sigma]_0=[\mathrm{tr}(\boldsymbol{\alpha}_{\mathbf{m}})/dV_p]=-[\mathrm{tr}(\mathbf{M})/dV_p]$ immediately follows [7]. Equation (7) is an approximate counterpart to this relation for viscous fluid hydrodynamics. We finally note that the electrostatic counterpart of $\mathbf{W}$ is the polarization tensor (not to be confused with the polarizability tensors $\boldsymbol{\alpha}_{\mathbf{e}}$ or $\boldsymbol{\alpha}_{\mathbf{m}}$). The hydrodynamic virtual mass is thus a kind of fluid polarization associated with the motion of bodies in fluids.

The final electrostatic-hydrodynamic analogy that we emphasize is the relation between electrostatic capacity C of a conducting particle and the translational friction coefficient f of a Brownian particle of the same shape. The total charge on a conducting particle is proportional to the potential on the body and to the electrostatic capacity C, which is itself a functional of the particle shape. Our units for capacity are chosen so that the capacity of a sphere in $d=3$ equals the sphere radius. Determination of C involves the solution of Laplace's equation with Dirichlet boundary conditions, as in the case of $\boldsymbol{\alpha}_{\mathbf{e}}$. The friction coefficient f of a Brownian particle is invariant to particle rotation since a diffusing particle samples all orientations as it moves over large distances. A formal angular averaging of the Oseen hydrodynamic interaction indicates that f is proportional to C [2,3,5,40],

$$f\approx 6\pi\eta(\text{dispersing liquid})C. \tag{10}$$

Therefore, within the angular averaging approximation, the capacity C of a conducting particle *equals* the hydrodynamic radius R_H of a Brownian particle of the same shape, since this latter is conventionally defined as $f/6\pi\eta$. Comparison between Eq. (10) and existing analytic results shows that it is accurate to about 1% generally and usually much better [2,3]. Equation (10) is exact for triaxial ellipsoids and a tabulation of exact values of C/f is given by Hubbard and Douglas [3]. There are many analogies relating C exactly to other transport properties (thermal capacity, Smoluchowski rate constant for diffusion-limited reactions, scattering length in quantum theory and acoustics, etc.) so that the determination of C has many further applications than those discussed in the present paper [2].

III. NUMERICAL PATH-INTEGRAL CALCULATION OF ELECTRICAL POLARIZABILITY AND CAPACITY

It has long been known that the capacity C can be calculated formally by averaging over random walk trajectories [41]. This interpretation of C is one of the classical results of probabilistic potential theory. The formal solution can be stated in a very simple way that we then generalize to a description of electrical polarizability α_e. We determine C mathematically by solving Laplace's equation $(\nabla^2\psi=0)$ with the boundary conditions $\psi=1$ on the boundary of the object Ω and $\psi\to 0$ at infinite distance [15]. The capacity defines the asymptotic decay of ψ at large distances, $\psi\sim C/R^{\delta-2}$ for $d>2$. We next consider random walks initiated at points outside of Ω and consider the probability that these paths hit Ω in some finite time. If the trajectory starts on Ω then the particle hits Ω with certainty while if the particle starts a long distance away then it hits with low probability. The equipotential surfaces of constant ψ for the charged conductor are also constant probability surfaces for hitting Ω. The charge density is proportional to the hit density of trajectories launched a large distance away. Explicit numerical calculation of C is facilitated by embedding Ω in some closed boundary for which Laplace's equation can be solved exactly, the simplest of which is a sphere [2,4]. We also employ the sphere embedding method in our calculation of $\boldsymbol{\alpha}_{\mathbf{e}}$ below.

The determination of $\boldsymbol{\alpha}_{\mathbf{e}}$ also involves the solution of Laplace's equation with Dirichlet boundary conditions, although of course $\boldsymbol{\alpha}_{\mathbf{e}}$ is a tensor. Tensors have not been considered previously by path-integral computation so our implementation of this calculation should have theoretical as well as practical interest.

We imagine that the body whose polarizability we wish to calculate sits near the origin and that two point charges of magnitude $-Q_+$ and $+Q_-$ are placed at sites $\pm L$ along the z axis. These point charges generate the external electric field. Of course, we require the external field to be uniform over length scales much larger than the body, which is achieved by letting $L\to+\infty$, $-Q_+\to-\infty$, and $Q_-\to+\infty$, in such a way that the electric field at the origin remains constant. Equivalently, we can imagine that Q_+ positive random walkers (''positrons'') and Q_- negative random walkers (''electrons'') are released, respectively, from the points at $\pm,L$ and that some of these eventually adsorb on the body.

We next consider a sphere of radius R centered at the origin. R is arbitrary as long as the body lies completely inside the sphere. All walkers that eventually reach the body must pass through the surface of the sphere. Our knowledge of the problem of a point charge outside a grounded spherical conductor lets us predict the distribution of random walkers passing through the sphere [4,30]. Specifically,

$$\sigma_\pm(\mathbf{r})=[Q_\pm\beta-3Q_\pm\beta^2]\rho_0(\mathbf{r})+3Q_\pm\beta^2\rho_\pm(\mathbf{r}), \tag{11}$$

gives the number density of ''positrons'' and ''electrons,'' respectively, that pass through the sphere. These are linear combinations of three normalized distribution functions defined on the surface of the sphere

$$\rho_0(\mathbf{r})=(4\pi R^2)^{-1}, \tag{12}$$

$$\rho_\pm(\mathbf{r})=(4\pi R^2)^{-1}(1\pm\cos\theta). \tag{13}$$

Here $\beta=R/L\ll 1$, and θ is the polar angle. Equation 11 is the $O(\beta^2)$ expansion of the more general formula [4,30], but since we take $L\to\infty$, only these terms are needed. These expansions indicate, for example, that of the Q_+ positrons emitted at $z=+L$, βQ_+ arrive at the sphere, and of these, $3Q_+\beta^2$ are distributed according to ρ_+, while the remainder are distributed uniformly.

Monte Carlo techniques can be used to estimate the statistics of the random walkers at all times following their arrival at the surface of the sphere. Launch a total of $N/2$ positrons from the sphere at R, with the initial sites selected

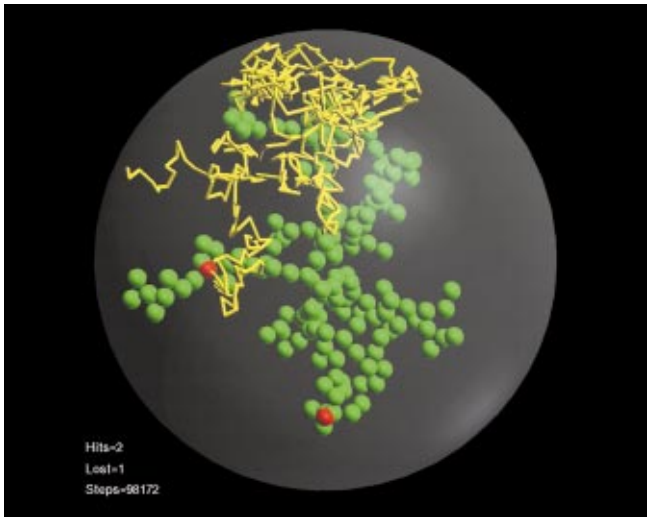

FIG. 2. (Color) Illustrative realization of a random walk sampling path launched from an enclosing surface. The object in this case is a model branched polymer where spheres are placed at the vertices of the ''graph'' describing the polymer. The fraction of random walk trajectories that hit the polymer rather than the launch sphere determines the electrostatic capacity. The electrostatic polarizability tensor is obtained similarly except that the launched random walks are assigned charges according to the position from which they are launched (see text for details).

according to the ρ_+ distribution. Define K_+ to be the number of these that adsorb onto the body, while the remainder are lost to ∞. Also accumulate the vector sum of all these K_+ contact points and call the sum V_+. Then launch $N/2$ electrons according to the distribution ρ_- and let K_- and V_- represent the number of contacts and sum of contact points, respectively. Technical details for doing such simulations have been worked out in a number of cases [2–4], and in the next section we describe several techniques. Finally, define

$$t=(K_+ + K_-)/N, \tag{14}$$

$$u=(K_+ - K_-)/N, \tag{15}$$

$$v=(V_+ + V_-)/N, \tag{16}$$

$$w=(V_+ - V_-)/N. \tag{17}$$

Furthermore, by placing electrons and positrons on an equal footing ($\rho_+ + \rho_- = 2\rho_0$), we accumulate statistics for the case in which random walkers are launched uniformly from the sphere. This is exactly the Monte Carlo procedure already developed for the electrostatic capacity [2–4]. Therefore, the capacity of the body is

$$C=tR. \tag{18}$$

The total positron charge that accumulates on the body is the sum

$$q_p = +[Q_+\beta - 3Q_+\beta^2]t + 3Q_+\beta^2(2K_+/N), \tag{19}$$

while the total electron charge is

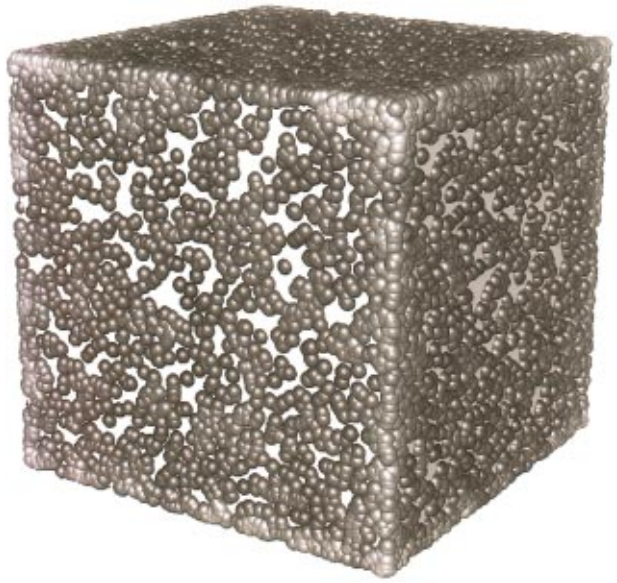

FIG. 3. (Color) Random walk hit density for a unit cube. The dark hemispherical patches represent 2000 hits on the cube by random walks launched from an enclosing sphere. Note the increased density (charge density) near the sharp corners of the cube where charge density becomes singular (in the limit of an infinite number of probing walks.) We estimate the capacity of the cube to be $C = 0.660\,69(2)$.

$$q_e = -[Q_-\beta - 3Q_-\beta^2]t - 3Q_-\beta^2(2K_-/N). \tag{20}$$

The total charge, $q_p + q_e$, must vanish to $O(\beta^2)$. This occurs if we set

$$Q_- = Q_+(1+6\beta u/t). \tag{21}$$

The total dipole moment is

$$\mu = +[Q_+\beta - 3Q_+\beta^2]v + 6Q_+\beta^2(V_+/N) - [Q_-\beta - 3Q_-\beta^2]v - 6Q_-\beta^2(V_-/N), \tag{22}$$

while the electric field inside R is parallel to the z axis with magnitude $(Q_+ + Q_-)/L^2$. Dividing one by the other gives three diagonal components of the polarizability tensor

$$(\alpha_{13}, \alpha_{23}, \alpha_{33}) = 12\pi R^2[\mathbf{w} - (u/t)\mathbf{v}]. \tag{23}$$

Of course, it would be possible to repeat the calculation with polarizations along the x axis and y axis to obtain all the other components of $\boldsymbol{\alpha}_\mathbf{e}$. However, with slight generalization, it is possible to accumulate statistics on all components in a single run. Launch a total of N walks from the sphere at R, with the initial site (x,y,z) chosen anywhere at random on the surface of the sphere. Each walker is assigned three independent charges: It is designated as an x positron with probability $(1+x/R)/2$, otherwise it is designated as an x electron, and similarly, it is given a y charge and a z-charge according to the values of the other two components. In analogy with the above, we define K_j^+ and K_j^- to be the number of j positrons and j electrons, respectively, that adsorb. We let V_{ij}^+ and V_{ij}^- represent the sums of the ith components of the

displacement vectors at which j positrons and j electrons adsorb. Then define $u_j=(K_j^+-K_j^-)/N$, $t=(K_j^++K_j^-)/N$ (t is independent of j), $v_{ij}=(V_{ij}^++V_{ij}^-)/N$, and $w_{ij}=(V_{ij}^+-V_{ij}^-)/N$. Then the expression for each component of $\boldsymbol{\alpha}_\mathbf{e}$ equals

$$\sigma_{ij}=12\pi R^2[w_{ij}-u_jv_{ij}/t], \tag{24}$$

while Eq. (18) still holds for the capacity.

IV. TECHNICAL DETAILS

A calculation generally proceeds through the following steps until N walkers total have been launched and their trajectories calculated [2–4]. Realizations of the process for a model aggregate and for a cube are shown in Figs. 2 and 3, respectively.

Step A. Initiate a new random walker somewhere on the sphere of radius R, the ''launch'' sphere, and assign its three charges.

Step B. Let $\mathbf{r}$ represent the current position of the walker. If $\mathbf{r}$ lies outside the launch sphere, move the random walker through time until it either returns to the launch sphere or wanders off to infinity. The standard Green's function for a point charge outside a conducting sphere is used [4,30].

Step C. If $\mathbf{r}$ lies on or inside the launch sphere, move the walker forward in time by any of several different algorithms. Several of these are given elsewhere [4], and several are presented below.

Step D. If the random walker is found on the surface of the body, accumulate the various sums $K_j^\pm$ and $V_{ij}^\pm$, then proceed from step A with a new walker. If it has wandered off to infinity, proceed from step A without accumulating any statistics. Otherwise proceed from step B with the same walker.

All the algorithms developed for step C above assume that the walker lies outside the body, but either on or inside the launch sphere. In general, we seek an efficient way of moving the walker forward in time until it hits the body. The following paragraphs give three techniques for accomplishing this.

The plane algorithm. For computations on convex polyhedra, one can move the walker ahead until it first makes contact with the plane that contains the nearest face of the polyhedron, using the Green's function for a charge near an infinite conducting plane [30]. With finite probability the walker will also be found on the face of the polyhedron and the trajectory will terminate at this step. Otherwise the computation continues as outlined above.

The Zeno algorithm. Let $D(\mathbf{r})$ represent the smallest distance from $\mathbf{r}$ to the surface of the body. Move the walker to a new site chosen at random on the surface of the sphere of radius $D(\mathbf{r})$ centered on $\mathbf{r}$ and then proceed with step D. Just as in Zeno's paradox, the walker never actually reaches the surface of the body, but it moves arbitrarily close. Therefore, we declare contact whenever $D(\mathbf{r})$ is less than some small distance ε. For complex bodies, $D(\mathbf{r})$ may be difficult to calculate, so it is difficult to make general statements about the efficiency of this algorithm. However, when computation of $D(\mathbf{r})$ is trivial it is very efficient. For the simplest shapes we are able to simulate 10^6 independent random walks in about 1.5 min on a Pentium III machine. Calculations on chains of 3200 beads (see below) were slower, requiring about 35 s to simulate only 10^3 walks. The Zeno algorithm is also extremely versatile. Since the only model-specific feature is the function $D(\mathbf{r})$, the same computer code can be applied universally simply by plugging in the appropriate $D(\mathbf{r})$ subroutine. The best statistics are obtained when we use the smallest possible launch sphere.

The lattice algorithm. We have also been interested in applying these techniques to lattice models of macromolecules and, therefore, have experimented with walks performed on the same lattice [42]. This approach is hampered by the absence of analytic Green's functions for lattice walks. One approach that works reasonably well is to begin by selecting a site at random in the continuum on the surface of the launch sphere, then jumping directly from there to the nearest lattice site. The walker then walks on the lattice until it either encounters the body or finds itself outside a second sphere, the ''turn-back'' sphere, concentric with the launch sphere, but with a radius larger by about ten lattice spacings. Then the walker is either returned to the launch sphere or permitted to escape to infinity using the continuum Green's function for a charge outside a conducting sphere [4,30]. If it is returned to the launch sphere, it once again jumps to the nearest lattice site and begins walking on the lattice. Generally, we find that this algorithm generates errors comparable to the ratio of the lattice spacing to the capacity so that accurate results can only be obtained by extrapolating to very fine grids. It works best if a bit is assigned to each lattice site to report whether or not that lattice site is part of the body. A virtue of both the plane and Zeno algorithms is the capacity to take larger steps when the walker is farther from the body. This particular implementation of the lattice algorithm lacks that feature and, therefore, its efficiency suffers somewhat.

V. ILLUSTRATIVE CALCULATIONS

In order to test the technique presented here, we have calculated capacities and polarizabilities of a number of bodies for which either exact results or independent numerical calculations are available. There are a limited number of shapes that permit exact analytic calculation of C and $\boldsymbol{\alpha}_\mathbf{e}$, including ellipsoids, tori, pairs of spheres at arbitrary separation, lenses, spindles, and bowls [43–45]. Numerical estimates, often of very high accuracy, of objects such as the regular polygons and polyhedra have also been reported [46–49].

In these calculations, we determined all nine components α_{eij} simultaneously according to Eq. (24). In all cases the resultant tensor had the expected ''structure,'' namely, components that were expected, on the basis of symmetry, either to be mutually equal or zero, were indeed so, to within sampling error. However, for the sake of brevity, all nine components will not be reported here. When the tensor degenerates to a scalar, we report only the value of $[\sigma]_\infty$. When the body has rotational symmetry about an axis, two values, $[\sigma]_\parallel$ and $[\sigma]_\perp$, representing axial and transverse contributions,

TABLE I. Zeno-algorithm calculations on spheres. r is the sphere radius, c is the position of sphere center, R is the radius of launch sphere, and N is the number of trajectories calculated.

r	c	R	N (Units of 10^8)	C/r	$[\sigma]_\infty$
1	(0,0,0)	1	1.00	1.000 00(0)	2.9999(2)
1	(0,0,0)	1.1	1.00	1.000 03(3)	3.0001(3)
1	(0,0,0)	1.5	1.00	1.000 07(8)	3.0005(5)
1	(1,1,0)	$1+\sqrt{2}$	1.00	1.0001(1)	3.001(1)
2	(0,0,0)	3	1.00	0.999 94(7)	2.9994(5)
0.1	(0,0,2)	5	1.06	1.0005(7)	3.0(1)
0.5	(0.5,0.5,0.5)	2	1.06	0.9997(2)	2.999(2)
0.2	(0,0,0)	4	1.28	0.9998(4)	3.04(2)

respectively, are reported. These may be defined as follows, assuming the rotation axis of the body is aligned with the z axis:

$$[\sigma]_\parallel=(\alpha_e)_{zz}/3V_p,[\sigma]_\perp=[(\alpha_e)_{xx}+(\alpha_e)_{yy}]/3V_p, \quad (25)$$

with $[\sigma]_\parallel+[\sigma]_\perp=[\sigma]_\infty$. Finally, for regular polygons and disks, $(\alpha_e)_{zz}=0$ while $(\alpha_e)_{xx}=(\alpha_e)_{yy}$, but $V_p=0$ and $[\sigma]_\infty$ diverges. Therefore, we report the single component $(\alpha_e)_{xx}=(\alpha_e)_{yy}$ in those cases.

Error estimates for all the following examples are calculated from fluctuations observed over a series of runs and are indicated by a single digit in parentheses following decimal data, and represent the uncertainty in the final digit. These error estimates do not include small systematic errors, which might arise, for example, from the finiteness of the contact cutoff ε or the imperfection of the random number generator. (This type of calculation may have independent interest as a physical model for testing random number generators [50]). We performed on the order of 10^8 trajectories in any given calculation, and found that this generally guarantees five-figure accuracy in the capacity and four-figure accuracy in the polarizability. Therefore, 10^6 trajectories should yield three- to four-figure accuracy, which is adequate in most cases.

A. Spheres

Capacities and polarizabilities for a number of different spheres were calculated by the Zeno algorithm, with calculations summarized in Table I. In all cases the contact cutoff was set at $\varepsilon=10^{-5}$. The results are in excellent agreement with the known results $C=r$ and $[\sigma]_\infty=3$. The results also demonstrate that the technique is independent of the size of the launch sphere and of the position of the body inside the launch sphere, although better statistics result if the launch sphere is chosen to fit as snugly as possible. Because the $D(\mathbf{r})$ calculation for spheres is trivial, each individual calculation of 10^8 trajectories requires less than 2 h of Pentium III processor time.

The lattice algorithm was also performed on a series of spheres in order to test its performance on a well-understood case. Two lattices, the diamond and the simple cubic, were employed. Length units for the two lattices are chosen so that the nearest-neighbor distance equals $3^{1/2}$ and 1, respectively. A lattice ''sphere'' of radius r is defined as all lattice sites (x,y,z) such that $x^2+y^2+z^2\leqslant r^2$. We performed a number of runs over a range of r values between 20 and 50 and for various values of the launch and turn-back radii. In all cases, the final results could be well represented by these expressions:

$$C/r=0.999-0.51/r \quad \text{(diamond)}, \quad (26)$$

$$C/r=1.001-0.37/r \quad \text{(simple cubic)}, \quad (27)$$

$$[\sigma]_\infty=2.994-4.5/r \quad \text{(diamond)}, \quad (28)$$

$$[\sigma]_\infty=3.003-3.1/r \quad \text{(simple cubic)}. \quad (29)$$

As expected, corrections to the asymptotic continuum limit are inversely proportional to r. The leading term extrapolates to a value accurate to about three significant digits, which is adequate for many applications.

B. Polyhedra

The cube is perhaps the most extensively studied shape for which no exact results exist. The calculation of the capacity of the cube has been characterized as ''one of the major unsolved problems of electrostatic theory'' [51] and distinguished mathematicians have said that ''there is little hope of obtaining an exact solution.'' [23,52] Interest in the cube derives both from practical applications and the vexing contrast between the simplicity of the boundary shape and the mathematical intractability of the electrostatic calculations. Calculation of the electrical polarizability is an even more difficult problem.

Our results for the five regular polyhedra are given in Table II. Table III summarizes various estimates of the capacity and the polarizability of the cube. Our capacity value for the cube is consistent with a previous random walk calculation by Given, Hubbard, and Douglas, using a somewhat different ''first-passage algorithm,'' [53] averaging over 4.7 $\times 10^9$ trajectories. It also compares well to the so-called surface charge method (SCM) result of Goto, Shi, and Yoshida [46] that utilizes a sophisticated extrapolation technique to account for inaccuracies in fields near sharp corners. Brown [54], using a finite differences technique, has reported capacity values for each of the five regular polyhedra that agree well with ours. Earlier moment method calculations by Reitan and Higgins [51] and by Cochran [55] can also be cited.

Calculations of the polarizability of the cube also have a long history. Edwards and Bladel [56], using an integral equation—boundary discretization method, obtained an impossibly low value. ($[\sigma]_\infty=3$ is known to be the lowest possible value and is only achieved by the sphere [57]). Herrick and Senior [57] then made an improved estimate by a similar method with a guess of about 1% accuracy. A more recent calculation by Eyges and Gianino [58] gives no error estimate.

The cube result by Douglas and Garboczi [7a] was obtained by finite element calculation using a periodic unit cell on a digital lattice (simple cubic) where no effort was made

TABLE II. Regular polyhedra. L is length of edge, R is radius of launch sphere, and N is the number of trajectories. Other numerical results for the capacity come from the work of Goto, Shi, and Yoshida [46] and of Brown [49]. Numerical estimates of $[\sigma]_\infty$ for the cube are from Herrick and Senior [57], Eyges and Gianino [58], and Douglas and Garboczi [7]. N.A. denotes ''no results available.''

Polyhedron	Algorithm	L	R	N (units of 10^8)	C/L $[\sigma]_\infty$ (this work)	C/L $[\sigma]_\infty$ (other results)
Tetrahedron	Zeno	$2\sqrt{2}$	$\sqrt{3}$	1.00	0.356 80(3) 5.029(1)	0.356 N.A.
Cube	Plane	1	0.87	2.58	0.660 69(2) 3.6437(6)	0.660 674 9(6) 3.40 to 3.72
Cube	Zeno	2	$\sqrt{3}$	0.93	0.660 72(4) 3.6446(5)	0.660 674 9(6) 3.40 to 3.72
Octahedron	Zeno	$\sqrt{2}$	1	0.94	0.509 45(3) 3.5509(2)	0.510 N.A.
Icosahedron	Zeno	1.051 46	1	1.00	0.815 84(3) 3.1305(4)	0.816 N.A.
Dodecahedron	Zeno	0.713 64	1	1.00	1.246 48 (5) 3.1779(3)	1.238 N.A.

to account for the effects of digital resolution. The effect of digital resolution can be handled very simply in a way analogous to that of the random walk algorithm on lattices. It has been found, as expected, that the deviation of the calculated properties from the ''true,'' infinite resolution result scale as $1/N$, where N is the number of pixels on the edge of the cubic unit cell [7b,7c]. Using this technique, we were able to greatly improve the finite element calculation and found a revised value of $[\sigma]_\infty = 3.63(4)$ for the cube. About three significant figures of accuracy result in this method, similar to the lattice random walk algorithm mentioned above. The revised finite element estimate of $[\sigma]_\infty$ is then consistent within numerical accuracy with the random walk calculation. This result is very encouraging and suggests that finite element calculations can be routinely used to estimate $[\sigma]_\infty$ for objects having modest shape complexity. The random walk method is advantageous when the boundary shape is complex, so that the computational methods are complementary.

TABLE III. Various estimates of the capacity and polarizability of the cube.

	Estimate	Citation
C/L	0.660 69(2)	This work.
	0.660 68(1)	Given, Hubbard, and Dougles [53]
	0.660 674 9(6)	Goto, Shi, and Yoshida [46]
	0.661	Brown [49]
	0.655	Reitan and Higgins [51]
	0.6596	Cochran [55]
$[\sigma]_\infty$	3.6437(6)	This work
	<2	Edwards and Bladel [56]
	3.54(3)	Herrick and Senior [57]
	3.40	Eyges and Gianino [58]
	3.72	Douglas and Garboczi [7]

We also studied the cube using the lattice algorithm, obtaining

$$C/L = 0.660 + 0.12/L \quad \text{(diamond)}, \tag{30}$$

$$C/L = 0.659 + 0.14/L \quad \text{(simple cubic)}, \tag{31}$$

$$[\sigma]_\infty = 3.64 + 1.5/L \quad \text{(diamond)}, \tag{32}$$

$$[\sigma]_\infty = 3.63 + 1.5/L \quad \text{(simple cubic)}, \tag{33}$$

The lattice path integration is again accurate to about three figures, after an $L \to \infty$ extrapolation. We believe it provides insight into the boundary discretization approximation of finite element techniques. Comparison with Eqs. (26) to (29) indicate that the $O(1/L)$ corrections are smaller for cubes than for spheres. In effect, the good approximation of the boundary achievable for the cube reduces the uncertainty in boundary detection, the counterpart of ε in the Zeno algorithm calculations.

The Zeno algorithm was also applied to the truncated icosahedron, the well-known 60-vertex polyhedron that is obtained by trisecting the vertices of the regular icosahedron and that represents both C_{60} fullerene molecules and soccer ball-shaped objects [59]. With $N = 1.22 \times 10^7$ and $\varepsilon = 10^{-5}$, we obtained $C/R = 0.957\,93(6)$, where R is the distance from the center to any one of the vertices, and $[\sigma]_\infty = 3.0409(8)$.

TABLE IV. Regular n gons and circular disks. n is number of sides, with $n=\infty$ indicating a circular disk; N is number of trajectories; r is the distance from center to vertex of polygon and also the radius of the launch sphere; and $(\alpha_e)_{xx}$ is the component of polarizability in the plane of the object. SCM indicates estimates by the extrapolated surface charge method of Goto, Shi, and Yoshida [46]. Ex indicates exact values [43,60].

n	N (units of 10^8)	C/r (this work)	C/r (other estimates or exact values)	$(\alpha_e)_{xx}/r^3$ (this work)	$(\alpha_e)_{xx}/r^3$ (exact values)
3	2.4	0.434 52(3)	0.434 521 1(4) (SCM)	1.8387(6)	N.A.
4	1.0	0.518 79(6)	0.518 718(2) (SCM)	2.943(1)	N.A.
5	1.0	0.559 28(4)	0.559 441(1) (SCM)	3.6437(5)	N.A.
6	2.4	0.582 02(3)	0.582 226 7(5) (SCM)	4.0911(7)	N.A.
7	2.4	0.596 07(3)	0.596 242 3(1) (SCM)	4.3889(5)	N.A.
8	2.4	0.605 43(3)	0.605 469 73(6) (SCM)	4.5889(6)	N.A.
∞	1.1	0.636 60(4)	$2/\pi=0.636\,620$ (Ex)	5.333(1)	$16/3=5.3333$ (Ex)

C. Polygons and disks

The approach works equally well on flat objects. Table IV summarizes the results for polygons and a circular disk. All our results in Table IV were obtained using the Zeno algorithm with $\varepsilon=10^{-5}$. Most of the other estimates cited in Table IV were done by an extrapolated SCM [46], which appears to be very accurate for simple shapes such as the polygons, and which agrees well with our results. The capacity of a circular disc is a classical problem in electrostatics, $C=2r/\pi$ [60], which compares well to our numerical estimate $C=[0.999\,97(6)](2r/\pi)$. The polarizability component in the plane of the disc is known to be $(\alpha_e)_{xx}=16r^3/3$ [43], while the normal component is zero. Our estimate is $(\alpha_e)_{xx}=[1.0000(3)](16r^3/3)$.

Like the cube, the electrostatic properties of the square have been of interest, but also impossible to calculate exactly, with a number of calculations of increasing sophistication. These are summarized in Table V. The estimate of Goto, Shi, and Yoshida [46] obtained using the extrapolated SCM is most accurate. Reitan and Higgins [61] earlier SCM estimate without extrapolation is less accurate. Solomon's [62] estimate and Maxwell's original estimate [15] are also noted.

D. Touching spheres

There are exact results for the capacity of two spheres of different radii that are either mutually tangent [54] or that overlap [45]. We computed capacities and polarizabilities of several pairs of touching spheres of respective radius r_1 and r_2 by the Zeno algorithm with $\varepsilon=10^{-5}$, and using a launch sphere of radius r_1+r_2. Results appear in Table VI.

TABLE V. Various estimates of the capacity of the square of side 1.

0.366 84 (4)	This work
0.366 789 2 (9)	Goto, Shi, and Yoshida [46]
0.362	Reitan and Higgins [61]
0.367	Solomon [62]
0.3607	Maxwell, cited in Ref. [15]

E. Right circular cylinders

The right circular cylinder is perhaps the most challenging shape for which exact results exist [47]. Table VII compares the results of the Zeno algorithm (with 10^8 trajectories for each cylinder and $\varepsilon=10^{-5}$) with exact numerical results. d and h represent the diameter and height of the cylinder, respectively, and the radius of the launch sphere was set at $[(d/2)^2+(h/2)^2]^{1/2}$. $C(0)$ is the capacity of a sphere having the same volume as the cylinder. The numerical agreement with the analytic calculations is generally good. The "exact" results are obtained numerically from complex expressions and we suspect, given the quality of our comparisons in other cases, that the inaccuracy observed in Table VI arises from the evaluation these expressions. We also note that exact analytic results exist [48] for $\boldsymbol{\alpha}_{\mathbf{m}}$ that should provide a good numerical test of path-integral calculations for the magnetic polarizability.

F. Tori

A torus is defined as the locus of points within a distance a of a circle of radius b, with $a\leqslant b$. Laplace's equation is separable in toroidal coordinates, which permits the development of series expansions for the capacity and the polarizability. Belevitch and Boersma [44] present numerically exact results for a number of different values of the ratio a/b. Especially accurate results are given in the "tight torus" limit, $a=b$ and the asymptotic behavior in the "thin loop" limit $a\ll b$ is also well understood [44]. Table VIII contrasts the results given in Ref. [44] with results of the Zeno algorithm, again with $N=10^8$ and $\varepsilon=10^{-5}$, for several different values of a and b. In all cases, the launch sphere had radius $a+b$, and $C(0)$ is the capacitance of a sphere having the same volume as the torus. Again the agreement is excellent.

VI. TRANSPORT PROPERTIES OF MACROMOLECULES

We now apply these techniques to the estimation of the transport properties of both linear polymers and dendrimers. This serves the dual purpose of displaying the power of our computational technique on bodies of complex shape and of obtaining results of significance in materials science.

TABLE VI. Touching spheres. Exact C values are from formulas given by Russell [54]. Exact values of $[\sigma]_{\parallel}$ and $[\sigma]_{\perp}$ are calculated from formulas given by Felderhof and Palaniappan [45].

r_1	r_2	N (units of 10^8)	C (simulated) C (exact)	$[\sigma]_{\parallel}$ (simulated) $[\sigma]_{\parallel}$ (exact)	$[\sigma]_{\perp}$ (simulated) $[\sigma]_{\perp}$ (exact)
1	1	1.12	1.386 41(8) 1.386 29	2.4036(6) 2.4041	1.8035(4) 1.8031
1	1/2	1.16	1.098 62(6) 1.098 61	1.7225(4) 1.7222	1.8999(4) 1.8995
1	1/3	1.16	1.039 69(5) 1.039 72	1.3225(3) 1.3228	1.9558(3) 1.9560
1	1/4	1.16	1.019 87(5) 1.019 92	1.1661(3) 1.1663	1.9779(3) 1.9779
1	1/5	1.15	1.011 41(4) 1.011 40	1.0960(2) 1.0961	1.9877(3) 1.9875
1	1/7	1.15	1.004 79(3) 1.004 76	1.0402(2) 1.0404	1.9952(3) 1.9950
1	1/9	1	1.002 49(3) 1.002 43	1.0206(2) 1.0206	1.9976(3) 1.9975
1	1/11	1.15	1.001 38(2) 1.00 140	1.0119(2) 1.0119	1.9984(2) 1.9986

A. Linear polymers

Chains of spherical beads are often used to model polymer chains. In fact, the connections between C and f and between $\langle \mathrm{tr}(\alpha_e)\rangle = \langle \alpha \rangle$ and $[\eta]$ were first recognized in calculations on chains of beads [5]. The Kirkwood-Riseman integral equation for the translational friction coefficient of a Gaussian polymer chain of beads reduces exactly to the integral equation for C in the angular averaging approximation.

TABLE VII. Right circular cylinders. d is cylinder diameter, h is cylinder height, and $C(0)$ is the capacity of sphere having same volume as the cylinder. Data in last column are numerical results of Smythe [47].

d	h	$C/C(0)$ $[\sigma]_{\parallel}$ $[\sigma]_{\perp}$ (this work)	$C/C(0)$ $[\sigma]_{\parallel}$ $[\sigma]_{\perp}$ (other estimates)
		1.060 97(4)	1.061
4	2	0.8109(2)	0.810 83
		2.8118(3)	2.8115
		1.040 91(4)	1.041
2	2	1.2863(2)	1.2871
		2.1127(3)	2.1138
		1.090 63(5)	1.091
1	2	2.3634(5)	2.3655
		1.7400(4)	1.7410
		1.220 51(9)	1.220
1	4	5.028(2)	5.0237
		1.5434(4)	1.5434
		1.448(2)	1.453
1	8	12.133(6)	N.A.
		1.4369(80)	N.A.

Consider a random chain of N spheres of radius 1 placed so that adjacent chain beads are touching. Noncontiguous beads are allowed to overlap. This model represents real polymer chains in solution at the theta temperature where attractive and repulsive intramolecular interactions largely compensate [63,64]. Ensembles containing at least 5000 statistically independent chains were generated for $N=25$, 50, 100, 200, 400, 800, 1600, 3200, and 6400. We launched 1000 trajectories from an enclosing launch sphere (see Fig. 2) at each chain in the ensemble utilizing the Zeno algorithm ($\varepsilon = 10^{-5}$). With only 1000 trajectories per chain, we estimate that there is 3 and 15% sampling error in the capacity and polarizability components, respectively, for any one chain. (These values were determined by launching many trajectories at a few chains, as in the examples discussed above). Nevertheless, the ensemble averages $\langle C \rangle$ and $\langle \alpha \rangle$ should be much more accurate since each average involves at least 5×10^6 probe trajectories. Computational time was linear in N, the bottleneck at large N being the computation of the function $D(\mathbf{r})$. Because of arbitrary overlap among spheres in the random walk chains, the volume V_p is neither easy to compute nor constant throughout the ensemble. However, the value of V_p is immaterial since it is more appropriate to consider the ensemble average of $[\eta]_M$.

We summarize our computations for C and the average polarizability in Fig. 4. The data (Table IX) are well represented by

TABLE VIII. Tori. Interior of torus is the set of points within a distance a of a circle of radius b. Exact results are from Bolevitch and Boersma. [44]

a	b	$u=a/b$	$C/C(0)$ $[\sigma]_{\parallel}$, $[\sigma]_{\perp}$ (this work)	$C/C(0)$ $[\sigma]_{\parallel}$, $[\sigma]_{\perp}$ (exact results)
			2.7263(2)	2.72608
1	20	0.05	0.6656(8), 87.92(2)	0.6662, 87.9008
			1.400 69(8)	1.400 68
1	4	0.25	0.6607(2), 8.209(1)	0.660 84, 8.208 81
			1.215 09(7)	1.215 18
2	5	0.40	0.6586(2), 4.9398(7)	0.658 99, 4.939 07
			1.151 20(6)	1.15119
1	2	0.50	0.6603(2), 4.0562(6)	0.660 160, 4.055 46
			1.070 58(4)	1.070 580
3	4	0.75	0.6734(1), 3.0767(4)	0.673 247, 3.076 312
			1.048 04(4)	1.048 077
9	10	0.90	0.6876(2), 2.8169(4)	0.687 524, 2.817 058
			1.038 63(4)	1.038 675 56
1	1	1.00	0.6992(2), 2.7054(4)	0.699 131 5, 2.705 461 4

$$\langle C\rangle \cong 0.657N^{1/2}+0.854, \tag{34}$$

$$\langle \mathrm{tr}(\boldsymbol{\alpha}_e)\rangle \cong 13.76N^{3/2}+49.2N, \tag{35}$$

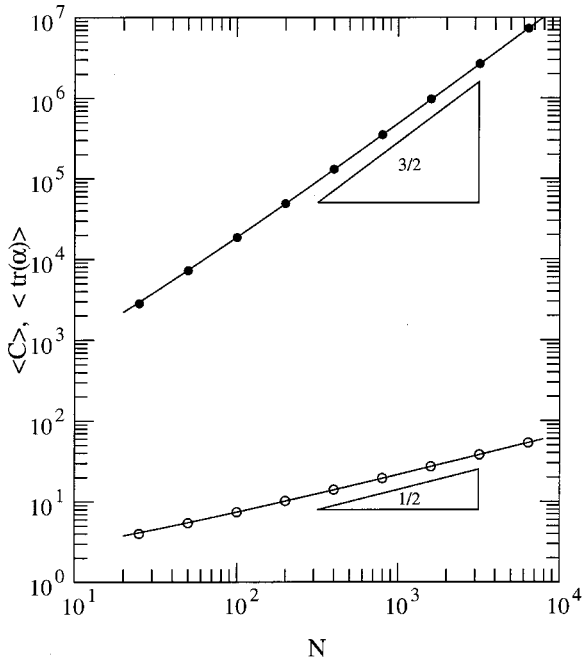

FIG. 4. The hydrodynamic radius and intrinsic viscosity of polymer chains are estimated, respectively, from the electrostatic capacity (○) and the polarizability (●) of perfect conductors having the same shape as the polymer chains. The mean electrostatic properties for ensembles of polymers are shown as functions of N. The fitted curves (solid lines) are given by Eqs. (34) and (35).

where $\langle\cdots\rangle$ denotes an ensemble average.

We use the relations $\langle C\rangle \cong R_h$ and Eq. (8) to estimate the hydrodynamic radius and intrinsic viscosity of polymer solutions. The application of these calculations to flexible molecules requires the assumption that the properties of a single chain with dynamic flexibility are equivalent to the ensemble average over a rigid set of molecules. Zimm has argued that this is valid [65]. Results are expressed relative to the radius of gyration R_g of the chain (root mean square distance of polymer segments from the center of mass [63,66]), which can be calculated exactly for this model [66]:

$$R_g=(2N/3)^{1/2}[1-N^{-2}]^{1/2}\approx(2N/3)^{1/2} \tag{36}$$

The ratio $\psi_h \equiv R_h/R_g$ for these chain models equals

$$\Psi_h=0.805+1.05N^{-1/2}, \tag{37}$$

TABLE IX. Chains of beads. N is chain length. Square brackets indicate powers of ten.

N	$\langle C\rangle$	$\langle \mathrm{tr}(\boldsymbol{\alpha}_e)\rangle$
25	4.01	2.83 [3]
50	5.44	7.22 [3]
100	7.41	1.851 [4]
200	10.19	4.90 [4]
400	14.06	1.306 [5]
800	19.50	3.51 [5]
1600	27.2	9.71 [5]
3200	38.0	2.66 [6]
6400	53.3	7.31 [6]

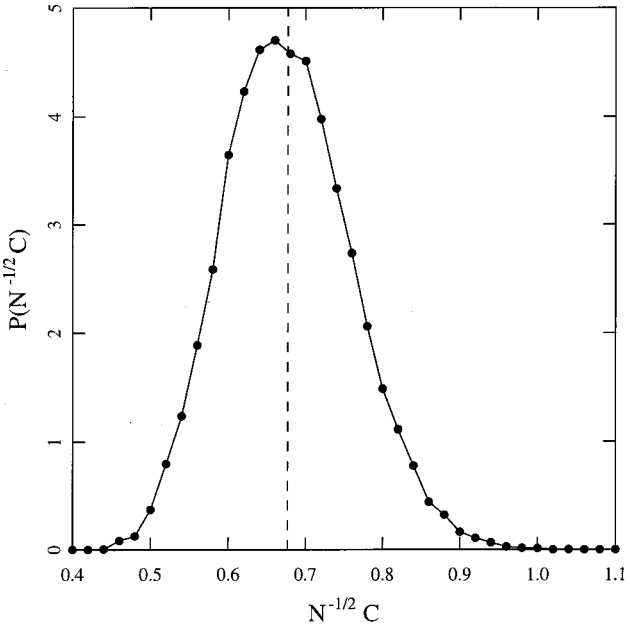

FIG. 5. Distribution function for the capacity C of flexible polymer chains including data for $N=800$, 1600, 3200, and 6400, normalized by $N^{1/2}$. The dashed line gives the value of the mean of the distribution.

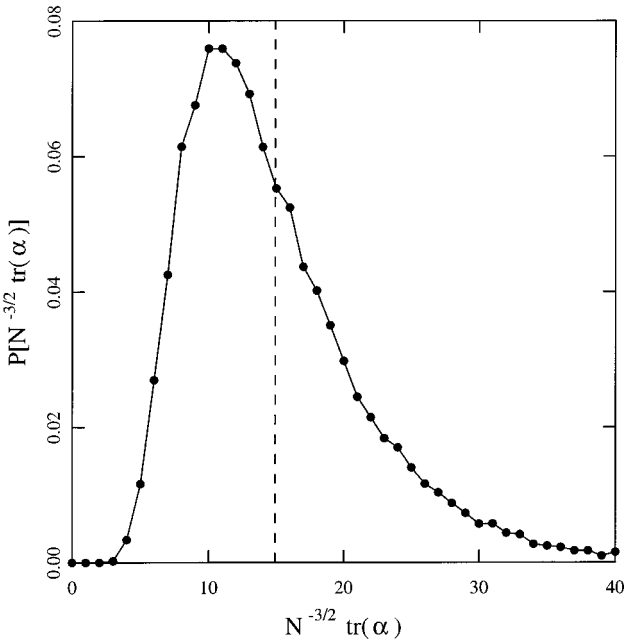

FIG. 6. Distribution function for the electrical polarizability trace $\mathrm{tr}(\alpha_e)$ of flexible polymer chains including data for $N=800$, 1600, 3200, and 6400, normalized by $N^{3/2}$. The dashed vertical line gives the value of the mean of the distribution.

and

$$M[\eta]_M R_g^{-3}=[6.66+23.8N^{-1/2}](1.00\pm 0.5). \quad (38)$$

The factor (1.00 ± 0.5) arises from the uncertainty in Eq. (8). The leading term in Eq. (38) is often reported in terms of the "Flory-Fox number," $\Phi=6^{-3/2}[\eta]_M MN_A/R_g^3$, where N_A is Avogadro's number. Our estimate of Φ is

$$\Phi=(2.73\pm 0.14)\times 10^{23}, \quad (39)$$

where the uncertainty again arises from the 5% uncertainty in Eq. (8). The best experimental estimates for ψ_h and Φ at the theta temperature are [67] 0.79 ± 0.04 and $(2.5\pm 0.1)\times 10^{23}$. Our present estimates also closely correspond to calculations for flexible random walk chains based on the Kirkwood-Riseman hydrodynamic equations without the configurational preaveraging approximation [65,68], $\psi_h(\mathrm{KR})=0.77\pm 0.03$ and $\Phi(\mathrm{KR})=(2.59\pm 0.18)\times 10^{23}$. (The stated uncertainties are estimates of sampling error. These values probably also contain systematic finite N errors.) The leading term in Eq. (37) is somewhat larger than the value $\psi_h\cong 0.77$ found in previous random walk simulations by Douglas, Zhou, and Hubbard [2] in which the bead radius was one quarter of the bond length rather than one half and for which $N=101$. This discrepancy may be due to finite N effects, even though this particular bead radius was employed because it exhibits relatively weak N dependence. Further discussion of ψ_h relative to previous theoretical estimates and measurements is given by Douglas and Freed [69].

This calculation of C and α_e also provides important information about the distribution of chain mobilities and shape fluctuations of flexible polymer chains. Computations based on conformational preaveraging generally overlook "unusual" members of the ensemble in favor of the most probable configurations. Relatively rare members of the ensemble can make a disproportionate contribution to any ensemble average because of the nonlinear nature of the random variable being averaged. Figure 5 shows the distribution of C for $N=800$, 1600, 3200, and 6400, with C normalized by $N^{1/2}$, which for long chains scales as R_g [see Eq. (36)]. The distribution seems to be *universal* with a small skewness. In Fig. 6, a similar normalization of the polarizability data shows greater skewness; the mean is about 50% larger than the mode. Therefore, fluctuation effects are expected to be more significant for the polarizability than for the capacity. The mean-field preaveraging approximation assumes that a "typical" or highly probable configuration is sufficient for the computation of ensemble averages. In the case of the random walk capacity, the true average C is substantially larger (about 10%) than the preaveraging estimate, suggesting that rare extended chains have a much larger friction cause the deviation. In the case of the polarizability, the deviation from preaveraging theory goes in the opposite direction. The preaveraged value of Φ is 2.87×10^{23}, larger than Eq. (39). This suggests that more compact chain configurations are the source of the deviation from mean-field theory. Thus, the sign of the departure from mean-field calculations is property dependent.

Chain swelling due to repulsive excluded volume interactions should produce narrower distribution functions for C and the components of $\boldsymbol{\alpha}_\mathbf{e}$. Previous numerical path-integration calculations indicate that fluctuations of C about its ensemble average is smaller for self-avoiding chains than for random walk chains [2]. The distribution of these prop-

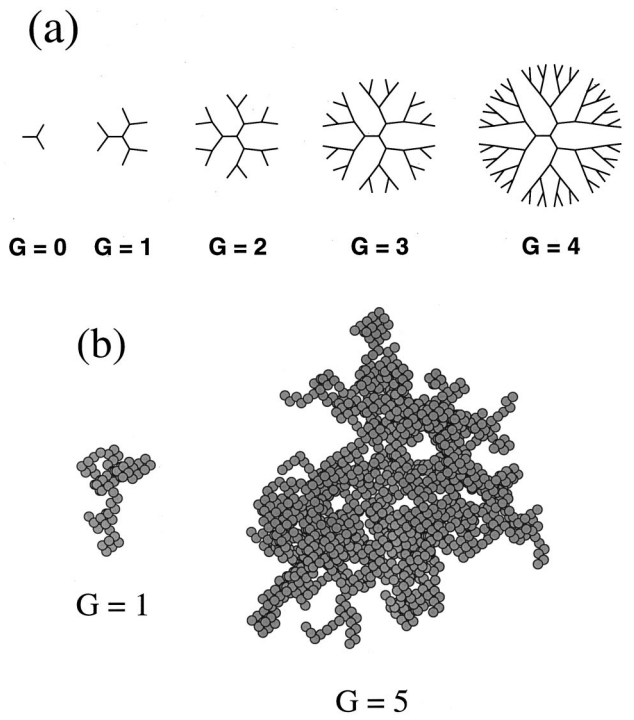

FIG. 7. Illustration of dendrimer molecules. (a) Topological structure. (b) Equilibrium structure of model dendrimer in real space.

erties and its dependence on excluded volume greatly complicates the calculation of transport properties. In principle, renormalization group theory provides a formal scheme for treating these fluctuation effects, but the method is less useful for these problems because of large ε-expansion coefficients [70]. While the method does indicate that preaveraging errors are substantially larger for simple random walk chains than for self-avoiding chains, the preaveraging errors predicted by second order ε-expansion[70] and the Kirkwood-Riseman model[68] are large in comparison to experiments and simulation [2]. The study of these properties should be very helpful in developing an adequate analytic theory of the hydrodynamics of polymers in dilute solutions. The fluctuations of the chain mobility accompanying the Brownian motion of the chain beads leads to modification of chain mobility by a ''Taylor dispersion'' [71] mechanism. An

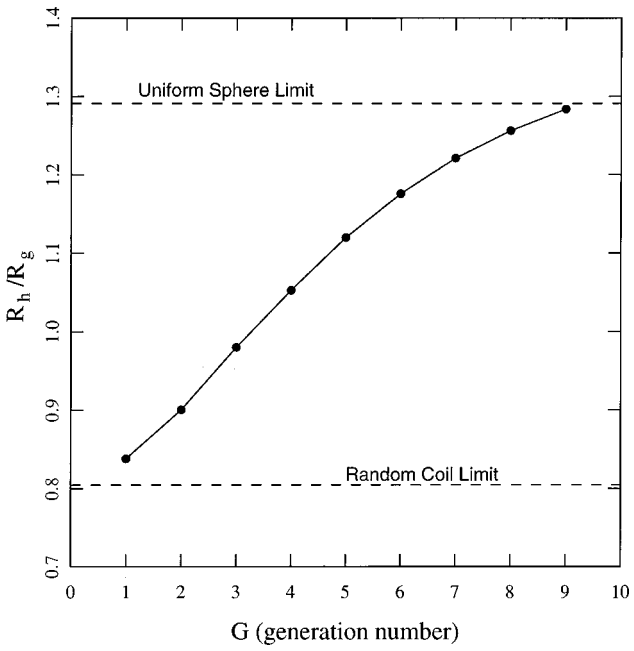

FIG. 8. Dimensionless hydrodynamic radius $\psi_h = R_h/R_g$ of dendrimers as function of generation number G.

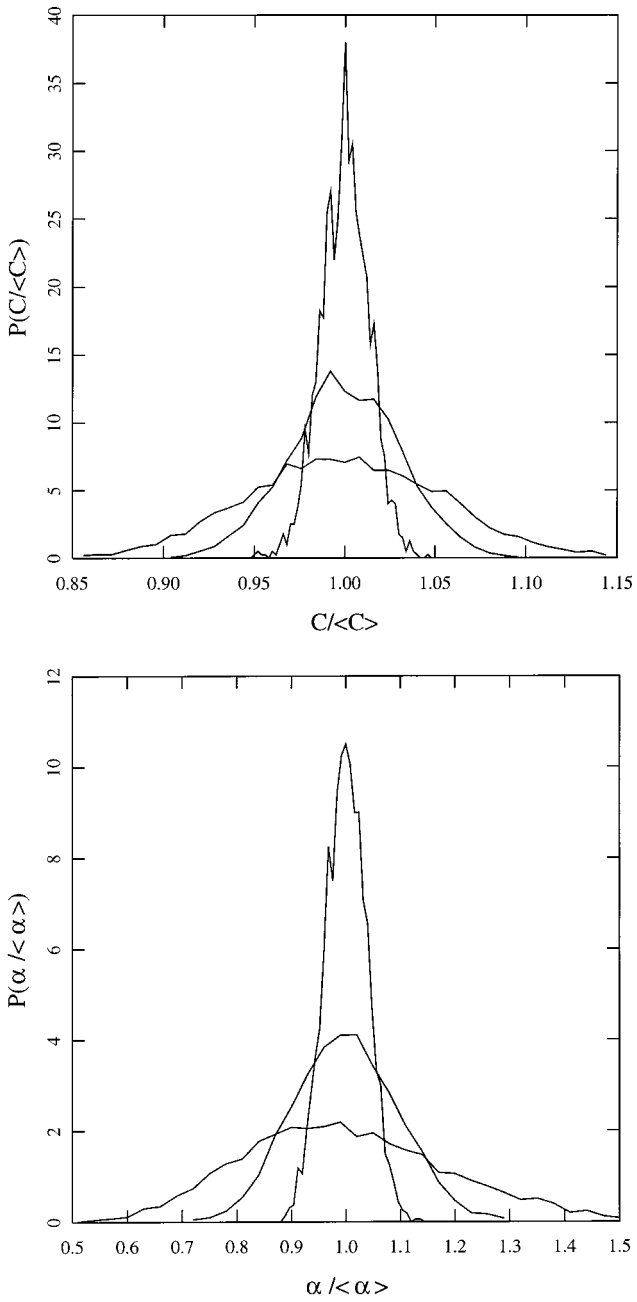

FIG. 9. Capacity (a) and polarizability (b) distributions of model dendrimers for generations $G=2$ (broadest), 5, and 8 (narrowest), normalized in each case by the mean. The distribution functions become sharper with increasing G, quantifying the approach to a spherical shape.

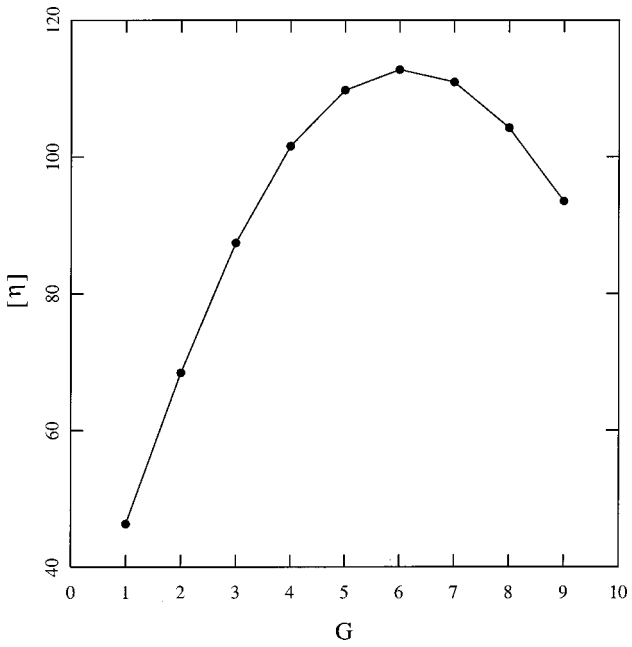

FIG. 10. Intrinsic viscosity of dendrimer molecules as a function of generation number G, with a maximum at $G=6$.

understanding of these distributions should be helpful in developing a quantitative description of this type of dispersion phenomenon.

B. Dendrimer polymers

Dendrimer molecules are highly branched polymers grown through a successive addition of multifunctional monomers. See Fig. 7 for an illustration of their topological form. During construction of each generation, multifunctional groups are added to saturation so that, unlike randomly branched polymers, the topological structure is nearly perfect. Undoubtedly, flexibility allows these molecules to relax to structures more uniformly distributed than the representation in Fig. 7. Indeed, much recent research is devoted to quantifying the geometrical structure of these polymers. At low generation number $G(G<4)$ the molecules resemble flexible star polymers and we can expect similarities to the flexible polymer calculations of the previous section. At higher $G(G>4)$ the branching constraints begin to predominate and structures with relatively uniform segmental densities form. Stearic interactions on added monomer restrict the number of generations that can be perfectly formed so that high generation $(4<G<13)$ dendrimers tend to be relatively spherical objects with a rough periphery and an interior with some segmental fluctuations. The high generation dendrimers resemble spongy round balls. In this section we report probabilistic calculations of the hydrodynamic radius R_h and intrinsic viscosity $[\eta]_M$ as a function of G. Some of these results have appeared in a previous work devoted to the characterization of dendrimer structure [42].

The dendrimer molecules are modeled on a diamond lattice to facilitate Monte Carlo simulation of dendrimer conformations for a large range of generations. A large library of these dendrimer structures has been generated and we directly apply our path-integration method (lattice algorithm) to the calculation of C and α_e. The mass of the model dendrimer is taken to equal the number of occupied lattice sites.

In Fig. 8 we show our results for $\psi_h=R_h/R_g$ as a function of G. Consistent with the discussion above, the magnitude of ψ_h is similar to values expected of flexible polymer chains when G is small, and to values expected of uniform spheres, $(5/3)^{1/2}\cong 1.29$, when G is large. Furthermore, the ratio $M[\eta]_M R_h^{-3}$ tends to $10\pi/3$, [42] as expected of spherical objects. These results all indicate a crossover from a random coil-like structure to a relatively uniform sphere with increasing G. Figure 9, showing the progression in the capacity and polarizability distributions as functions of generation number, further supports this picture. At low G there are large shape fluctuations, but the distributions become narrower as G increases. The standard deviation in C varies from about 6% to about 1% of the mean as G varies from 1 to 9, while the standard deviation in $\mathrm{tr}(\boldsymbol{\alpha}_\mathbf{e})$ varies from about 22% to 3% over the same range of G values. At $G=2$, the $\mathrm{tr}(\boldsymbol{\alpha}_\mathbf{e})$ distribution is slightly skewed and asymmetric, with mean and mode differing by about 7%.

Another signature of an increasing dendrimer compactness can be seen in the dependence of $[\eta]_M$ on G. Figure 10 shows that $[\eta]_M$ passes through a maximum at $G=6$. Maxima in $[\eta]_M$ vs G are familiar in the literature, occurring usually around $G=4$ to 6 [72]. In our units, a dense-packed sphere on this lattice would have $[\eta]_M=20$, since $V/M=8$ and $[\eta]=5/2$. The values in Fig. 10 are all considerably greater than this because the dendrimer is not dense packed. Indeed $20/[\eta]_M$ can be taken as an estimate of the internal packing fraction. This also illustrates that relatively large intrinsic viscosities can be achieved using relatively porous, symmetric objects. (See also Ref. [7])

VII. CONCLUSION

We have developed a general algorithm for simultaneously calculating the capacity C and electric polarizability tensor $\boldsymbol{\alpha}_\mathbf{e}$ of conducting objects having general shape. These shape functionals have many applications to the scattering of light and sound and are also important for describing effective properties of particle dispersions and transport properties of macromolecules. We estimate the translational friction coefficient and intrinsic viscosity of flexible linear polymers and of dendrimers. We also obtain the distribution functions for C and the trace of $\boldsymbol{\alpha}_\mathbf{e}$ for flexible chains and dendrimer molecules. These distributions are broad for flexible molecules, but become narrower in dendrimer molecules of increasing generation number. We also calculate C and $\boldsymbol{\alpha}_\mathbf{e}$ for model shapes for which independent calculations are available (spheres, polyhedra, tori, regular polygons, touching spheres, and circular cylinders) in order to establish the accuracy of our computational method. The numerical path-integral method proves to be quite flexible and especially efficient for complex-shaped particles and should have many biological and materials science applications.

[1] J. F. Douglas and A. Friedman, *Coping with Complex Boundaries*, IMA Series on Mathematics and its Applications Vol. 67 (Springer, New York, 1995), p. 166.
[2] J. F. Douglas, H.-X. Zhou, and J. B. Hubbard, Phys. Rev. E **49**, 5319 (1994).
[3] J. B. Hubbard and J. F. Douglas, Phys. Rev. E **47**, 2986 (1993).
[4] H.-X. Zhou, A. Szabo, J. F. Douglas, and J. B. Hubbard, J. Chem. Phys. **100**, 3821 (1994); B. A. Luty, J. A. Mc Cammon, and H.-X. Zhou, *ibid.* **97**, 5682 (1992); J. A. Given, J. B. Hubbard, and J. F. Douglas, *ibid.* **106**, 3761 (1997).
[5] J. F. Douglas, Adv. Chem. Phys. **102**, 121 (1997).
[6] F. Y. Hunt, J. F. Douglas, and J. Bernal, J. Math. Phys. **36**, 2386 (1995).
[7] (a) J. F. Douglas and E. J. Garboczi, Adv. Chem. Phys. **91**, 85 (1995); (b) A. P. Roberts and E. J. Garboczi, J. Am. Ceram. Soc. Bull. **83**, 3041 (2000); (c) E. J. Garboczi, Cem. Concr. Res. (to be published).
[8] E. J. Garboczi and J. F. Douglas, Phys. Rev. E **53**, 6169 (1996).
[9] J. W. Strutt (Lord Rayleigh), Philos. Mag. **44**, 28 (1897).
[10] J. B. Keller, R. E. Kleinman, and T. B. A. Senior, J. Inst. Math. Appl. **9**, 14 (1974).
[11] T. B. A. Senior, Radio Sci. **11**, 477 (1976); R. E. Kleinman and T. B. A. Senior, *ibid.* **7**, 937 (1972); T. B. A. Senior and R. E. Kleinman, IEEE Trans. Aerosp. Electron. Syst. **11**, 672 (1975); D. S. Jones, J. Inst. Math. Appl. **23**, 421 (1979); T. S. Angel and R. E. Kleinman, Radio Sci. **22**, 1120 (1982); K. S. H. Lee, *ibid.* **22**, 1235 (1987); G. Dassios and R. E. Kleinman, SIAM Rev. **31**, 565 (1989).
[12] J. Van Bladel, J. Sound Vib. **6**, 386 (1967); **8**, 186 (1968); J. Acoust. Soc. Am. **44**, 1069 (1968); T. B. A. Senior, *ibid.* **53**, 742 (1973); D. S. Jones, Proc. R. Soc. Edinburgh, Sect. A: Math. **83**, 245 (1979); V. I. Fabrikant, J. Sound Vib. **111**, 742 (1986); **121**, 1 (1988).
[13] H. Bethe, Phys. Rev. **66**, 163 (1944); C. J. Bouwkamp, Rep. Prog. Phys. **17**, 35 (1954); J. Van Bladel, Radio Sci. **14**, 319 (1979); F. DE Meulenaere and J. Van Bladel, IEEE Trans. Antennas Propag. **25**, 198 (1977); D. L. Jaggard and C. H. Papas, Appl. Phys. **15**, 21 (1978); S. B. Cohn, Proc. IRE **39**, 1416 (1951); J. Appl. Phys. **20**, 257 (1949); **22**, 628 (1951); E. K. Okon and R. F. Harrington, IEEE Trans. Electromagn. Compat. **23**, 359 (1981); E. Avras, IEEE Trans. Antennas Propag. **31**, 719 (1983); N. A. Mc Donald, IEEE Trans. Microwave Theory Tech. **33**, 1146 (1985); **35**, 20 (1987); V. I. Fabrikant, J. Phys. A **20**, 323 (1987).
[14] J. Van Bladel, J. Sound Vib. **6**, 386 (1967); **8**, 186 (1968); W. E. Williams, *ibid.* **13**, 37 (1970); V. I. Fabrikant, *ibid.* **121**, 1 (1988); R. De Smedt, *ibid.* **75**, 371 (1981).
[15] G. Pólya and G. Szegö, *Isoperimetric Inequalities in Mathematical Physics*, Annals of Mathematics Studies, Vol. 27 (Princeton University Press, Princeton, 1951); L. E. Payne, SIAM Rev. **9**, 453 (1967).
[16] J. F. Douglas, J. Roovers, and K. F. Freed, Macromolecules **23**, 4168 (1990).
[17] The ''hydrokinetic analogy'' relating the hydrodynamics of inviscid fluids and the theory of magnetism is utilized extensively by Kelvin. See: W. M. Thompson (Lord Kelvin), *Reprints on Electricity and Magnetism* (MacMillan, London, 1884), Secs. 16–17, Article 32.
[18] G. I. Taylor, Proc. R. Soc. London, Ser. A **120**, 13 (1928); *ibid.* **120**, 260 (1928); G. Birkoff, *Hydrodynamics: A Study of Logic, Fact and Similitude* (Princeton University Press, Princeton, NJ, 1960), Chap. 6; G. Pólya, Proc. Natl. Acad. Sci. U.S.A. **33**, 218 (1947); S. Szegö, Duke Math. J. **16**, 209 (1949); E. B. Moullin, Proc. Phys. Soc. London **29**, 400 (1928); G. Cook, Philos. Mag. **34**, 350 (1920); K. Thompson, Am. J. Phys. **56**, 1043 (1988).
[19] R. Roscoe, Philos. Mag. **40**, 338 (1949); D. L. Jain and R. P. Kanwal, J. Anal. Math. **25**, 107 (1972).
[20] R. P. Kanwal, J. Fluid Mech. **10**, 17 (1960).
[21] L. E. Payne, Q. Appl. Math. **10**, 197 (1952); A. Weinstein, Bull. Am. Math. Soc. **50**, 20 (1953); L. E. Payne and A. Weinstein, Pac. J. Math. **2**, 633 (1960); G. W. Weiss and L. E. Payne, J. Appl. Phys. **25**, 1321 (1954).
[22] O. Heaviside, Philos. Mag. **23**, 10 (1887).
[23] J. W. Strutt (Lord Rayleigh), *Theory of Sound* (Dover, New York, 1945), Vol. 2; E. O. Tuck, Adv. Appl. Math. **14**, 89 (1974).
[24] H. Hasimoto, J. Phys. Soc. Jpn. **13**, 633 (1958); C. Y. Wang, Phys. Fluids A **5**, 1113 (1993).
[25] G. Wallis, Multiphase Sci. Technol. **5**, 239 (1976); P. Smereka and G. W. Milton, J. Fluid Mech. **233**, 65 (1991); A. S. Sangani, D. Z. Zhang, and A. Prosperetti, Phys. Fluids A **3**, 2955 (1991); X. Cai and G. B. Wallis, Phys. Fluids A **5**, 1614 (1993).
[26] J. W. Strutt (Lord Rayleigh), *Theory of Sound* (Dover, New York, 1945), Vol. 1; R. Hill and G. Power, Q. J. Mech. Appl. Math. **9**, 313 (1956); E. Guth, J. Appl. Phys. **16**, 21 (1945); J. S. Chong, E. B. Christiansen, and A. D. Baer, J. Polym. Sci. **15**, 2007 (1971); N. Phan-Thien, J. Elast. **32**, 243 (1993); S. C. Hunter, Proc. Ed. Math Soc. **15**, 55 (1967); M. Gordon, S. C. Hunter, J. A. Love, and T. C. Ward, Nature (London) **217**, 735 (1968); R. P. Kanwal, Q. Appl. Math. **8**, 146 (1955); M. S. Jhon, R. J. Metz, and K. F. Freed, J. Stat. Phys. **52**, 1325 (1988).
[27] G. K. Batchelor, Annu. Rev. Fluid Mech. **6**, 227 (1974).
[28] S. Torquato, Appl. Mech. Rev. **44**, 37 (1991).
[29] M. Fixman, J. Phys. Chem. **88**, 6472 (1984).
[30] J. D. Jackson, *Classical Electrodynamics*, 2nd ed. (Wiley, New York, 1975); J. A. Stratton, *Electromagnetic Theory* (McGraw-Hill, New York, 1941).
[31] A. Lakhtakia, Chem. Phys. Lett. **174**, 583 (1990).
[32] J. C. Maxwell, *A Treatise on Electricity and Magnetism* (Dover, New York, 1954).
[33] A. S. Sangani, SIAM (Soc. Ind. Appl. Math.) J. Appl. Math. **50**, 64 (1990).
[34] G. K. Batchelor, J. Fluid Mech. **41**, 545 (1970); G. K. Batchelor, *ibid.* **46**, 813 (1971); G. K. Batchelor and G. K. Green, *ibid.* **56**, 375 (1972); J. M. Rallison, *ibid.* **88**, 529 (1978); D. J. Jeffrey and A. Acrivos, AIChE J. **22**, 417 (1976); S. Kim and S.-Y. Lu, Int. J. Multiphase Flow **13**, 837 (1987); P. Pakdel, J. Rheol. **35**, 797 (1991).
[35] A. Einstein, Ann. Phys. (Leipzig) **19**, 289 (1906); **34**, 591 (1911); J. F. Brady, Int. J. Multiphase Flow **10**, 113 (1984).
[36] S. Haber and H. Brenner, J. Colloid Interface Sci. **97**, 496 (1984); J. M. Rallison, J. Fluid Mech. **84**, 237 (1978).
[37] A slender body is taken to have at least one of the dimensions governing the scale of the body to be smaller than the largest scale by at least a factor of 5. A globular body is more sym-

metric in shape and we arbitrarily define such a body to have relative dimensions that do not differ more than 50%.

[38] J. L. Bouillot, C. Camoin, M. Belzons, R. Blanc, and E. Guyon, Adv. Colloid Interface Sci. **17**, 299 (1982).

[39] A. J. C. Ladd, M. E. Colvin, and D. Frenkel, Phys. Rev. Lett. **60**, 975 (1988).

[40] The combination of bounds on the sedimentation coefficient [H. F. Weinberger, J. Fluid Mech. **52**, 321 (1972)] of nonskew bodies of general shape and Brenner's expression [H. Brenner, Adv. Chem. Phys. **6**, 287 (1966)] relating f to the average of the reciprocal diagonal components of the translational friction tensor indicates the bound, $f \geqslant 6\ \pi\ \eta$ (dispersing liquid) C for nonskew bodies. Rigorous bounds of the matrix elements of the shearing matrix in terms of C and the components of $\boldsymbol{\alpha}_{\mathbf{e}}$ [A. Nir, H. F. Weinberger, and A. Acrivos, J. Fluid Mech. **68**, 739 (1979)] have also been obtained.

[41] G. A. Hunt, Trans. Am. Math. Soc. **81**, 294 (1956); P. Erdös and S. J. Taylor, Acta Math. Acad. Sci. Hung. **11**, 137 (1960); K. Ito and Mckean, J. Math. **4**, 119 (1960); Z. Ciesielsky, Bull. Acad. Pol. Sci., Ser. Sci., Math., Astron. Phys. **12**, 265 (1964); K. L. Chung Ann. Inst. Fourier **23**, 313 (1973); F. Spitzer, Z. Wahrscheinlichkeitstheor. Verwandte Geb. **3**, 110 (1964); M. Kac, Rocky Mt. J. Math. **4**, 3 (1974).

[42] M. L. Mansfield, Macromolecules **33**, 8043 (2000).

[43] M. Schiffer and G. Szegö, Trans. Am. Math. Soc. **67**, 130 (1949).

[44] V. Belevitch and J. Boersma, Philips J. Res. **38**, 79 (1983).

[45] B. U. Felderhof and D. Palaniappan, J. Appl. Phys. **86**, 6501 (1999); **88**, 4947 (2000).

[46] E. Goto, Y. Shi, and N. Yoshida, J. Comput. Phys. **100**, 105 (1992).

[47] W. W. Smythe, J. Appl. Phys. **33**, 2966 (1962); T. T. Taylor, J. Res. Natl. Bur. Stand., Sect. B **64B**, 135 (1960); See, also, P. Q. Wang, IEEE Trans. Antennas Propag. **32**, 956 (1984).

[48] T. T. Taylor, J. Res. Natl. Bur. Stand., Sect. B **64B**, 199 (1960).

[49] C. S. Brown, Comput. Math. Appl. **20**, 43 (1990).

[50] I. Vattulainen, T. Ala-Nissila, and K. Kankaala, Phys. Rev. A **52**, 3205 (1995).

[51] D. Reitan and T. J. Higgins, J. Appl. Phys. **22**, 223 (1951).

[52] G. Pólya, Am. Math. Monthly **54**, 201 (1947).

[53] J. A. Given, J. B. Hubbard, and J. F. Douglas, J. Chem. Phys. **106**, 3761 (1997).

[54] A. Russell, Proc. Phys. Soc. London **37**, 1925 (1925); Poisson, Mem. de l'Instit. **1**, 1 (1811); **2**, 163 (1811).

[55] G. D. Cochran, Doctoral dissertation, University of Michigan, 1967.

[56] T. W. Edwards and J. Van Bladel, Appl. Sci. Res., Sect. B **9**, 151 (1961); See, also, K. Mei and J. Van Bladel, IEEE Trans. Antennas Propag. **11**, 52 (1963).

[57] D. F. Herrick and T. A. Senior, IEEE Trans. Antennas Propag. **25**, 590 (1977); M. Shiffer, C. R. Acad. Sci. III **244**, 3118 (1957); L. E. Payne and H. F. Weinberger, Bull. Am. Math. Soc. **59**, 244 (1953).

[58] L. Eyges and P. Gianino, IEEE Trans. Antennas Propag. **27**, 557 (1979).

[59] B. Kostant, Not. Am. Math. Soc. **42**, 959 (1995).

[60] J. Jeans, *The Mathematical Theory of Electricity and Magnetism*, 5th ed. (Cambridge University Press, London, 1941).

[61] D. K. Reitan and T. J. Higgins, Trans. AIEE, Part 1 **75**, 761 (1957).

[62] L. Solomon, C. R. Acad. Sci. III **258**, 64 (1964).

[63] H. Yamakawa, *Modern Theory of Polymer Solutions* (Harpers, New York, 1969).

[64] P.-G. deGennes, *Scaling Concepts in Polymer Physics* (Cornell University Press, Ithaca, NY, 1979).

[65] B. H. Zimm, Macromolecules **13**, 592 (1980); J. G. de la Torre, A. Jimenez, and J. Freire, Macromolecules **15**, 148 (1982).

[66] P. J. Flory, *Statistical Mechanics of Chain Molecules* (Wiley, New York, 1969).

[67] M. Schmidt and W. Burchard, Macromolecules **14**, 210 (1981); S. Park, T. Chang, and I. H. Park, Macromolecules **24**, 5729 (1991); Y. Miyaki, Y. Einaga, H. Fujita, and M. Fakuda, Macromolecules **13**, 588 (1980).

[68] J. G. Kirkwood and J. Riseman, J. Chem. Phys. **16**, 565 (1948).

[69] J. F. Douglas and K. F. Freed, Macromolecules **27**, 6088 (1994).

[70] S. Q. Wang, J. F. Douglas, and K. F. Freed, J. Chem. Phys. **85**, 3674 (1986); **87**, 1346 (1987).

[71] H. Brenner, A. Nadim, and S. Haber, J. Fluid Mech. **183**, 511 (1987); I. Frenkel, F. Mancini, and H. Brenner, J. Chem. Phys. **95**, 8636 (1991).

[72] D. A. Tomalia, D. M. Hedstrand, and L. R. Wilson, *Encycloclopedia of Polymer Science and Engineering*, 2nd ed. (Wiley, New York, 1990); T. H. Mourey, S. R. Turner, J. M. J. Frechet, C. J. Hawker, and K. L. Wooley, Macromolecules **25**, 2401 (1992).